Supporting Information

A Cathode-Integrated Sulfur-Deficient Co_9S_8 Catalytic Interlayer for the Reutilization of "Lost" Polysulfides in Lithium-Sulfur Batteries

Haibin Lin, Shengliang Zhang, Tianran Zhang, Sheng Cao, Hualin Ye, Qiaofeng Yao, Guangyuan Wesley Zheng* and Jim Yang Lee*

Department of Chemical and Biomolecular Engineering, National University of Singapore, 10 Kent Ridge Crescent, Singapore 119260, Singapore.

Corresponding addresses: cheleejy@ nus.edu.sg; chezg@nus.edu.sg

Table S1 Elemental compositions of Co_9S_8/CNT treated at different temperature in hydrogen.

	precusor	500 °C	700 °C	900 °C
Co (%)	52.89	55.84	60.11	66.16
S (%)	47.11	44.16	39.89	33.84

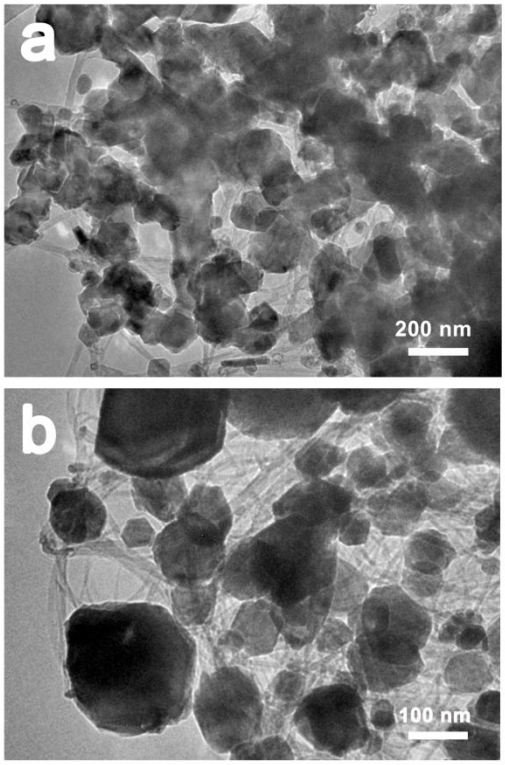

Figure S1. TEM image of Co_9S_8/CNT composite heat-treated at 900 ^oC in hydrogen.

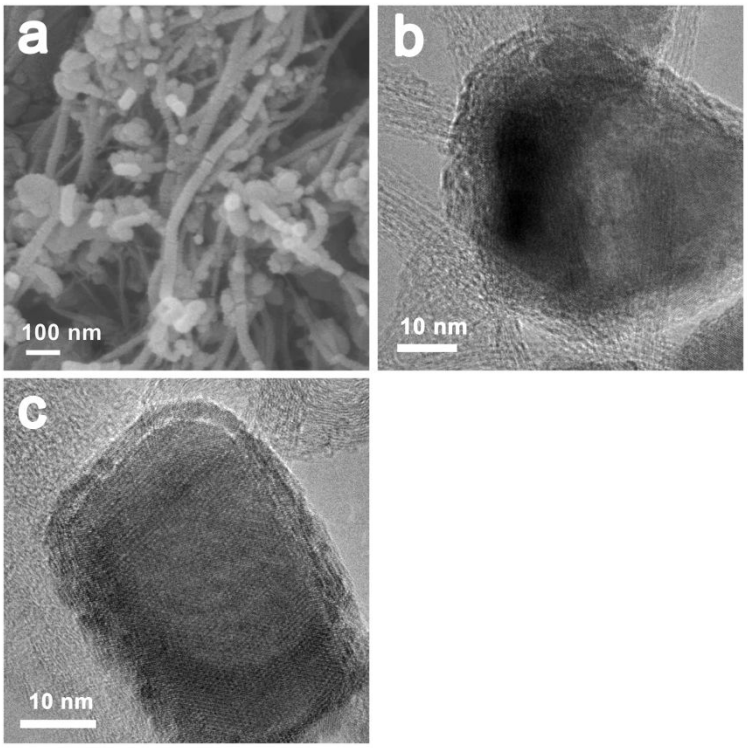

Figure S2. (a) FESEM and (b-c) TEM images of the Co_9S_{8-x}/CNT prepared by heating Co_9S_8/CNT composite at 700 ^oC in hydrogen.

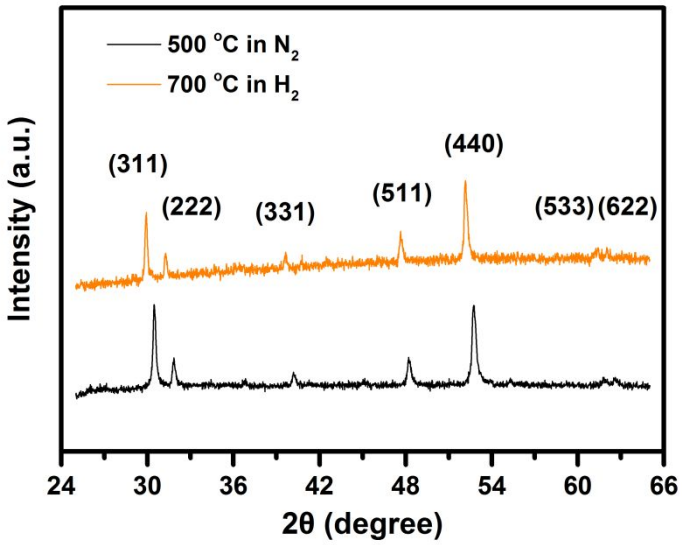

Figure S3. XRD pattern of the Co_9S_8/CNT treated at 500 °C in nitrogen and at 700 °C in hydrogen atmosphere.

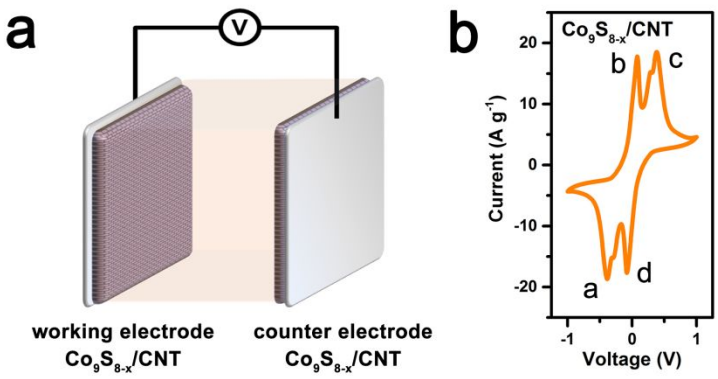

c

Peak a

Reaction on working electrode: $S_6^{2-} + 10e^- + 12Li^+ \rightarrow 6Li_2S$

Reaction on counter electrode: $4S_6^{2-} - 8e^- \rightarrow 3S_8$

Peak b

Reaction on working electrode: $6Li_2S - 10e^- \rightarrow S_6^{2-} + 12Li^+$

Reaction on counter electrode: $3S_8 + 8e^- \rightarrow 4S_6^{2-}$

Peak c

Reaction on working electrode: $4S_6^{2-} - 8e^- \rightarrow 3S_8$

Reaction on counter electrode: $S_6^{2-} + 10e^- + 12Li^+ \rightarrow 6Li_2S$

Peak d

Reaction on working electrode: $3S_8 + 8e^- \rightarrow 4S_6^{2-}$

Reaction on counter electrode: $6Li_2S - 10e^- \rightarrow S_6^{2-} + 12Li^+$

Figure S4. (a) Schematic of a symmetric cell, (b) cyclic voltammograms of the symmetric cell with a Co_9S_{8-x}/CNT catalyst and (c) illustration of the electrode reactions for the redox peaks.

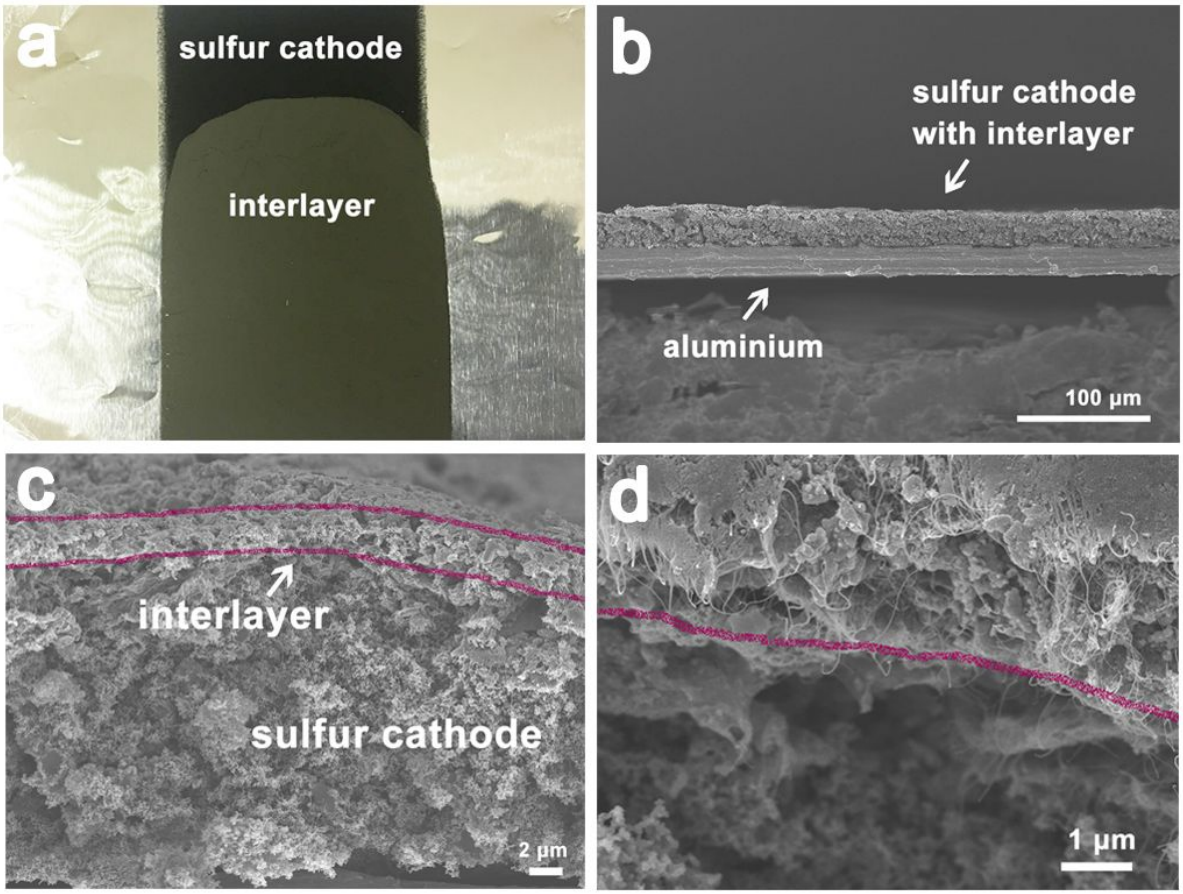

Figure S5. Characterization of the Co_9S_{8-x}/CNT interlayer on the sulfur cathode. (a) Photograph and (b-d) FESEM images of the sulfur cathode with Co_9S_{8-x}/CNT interlayer.

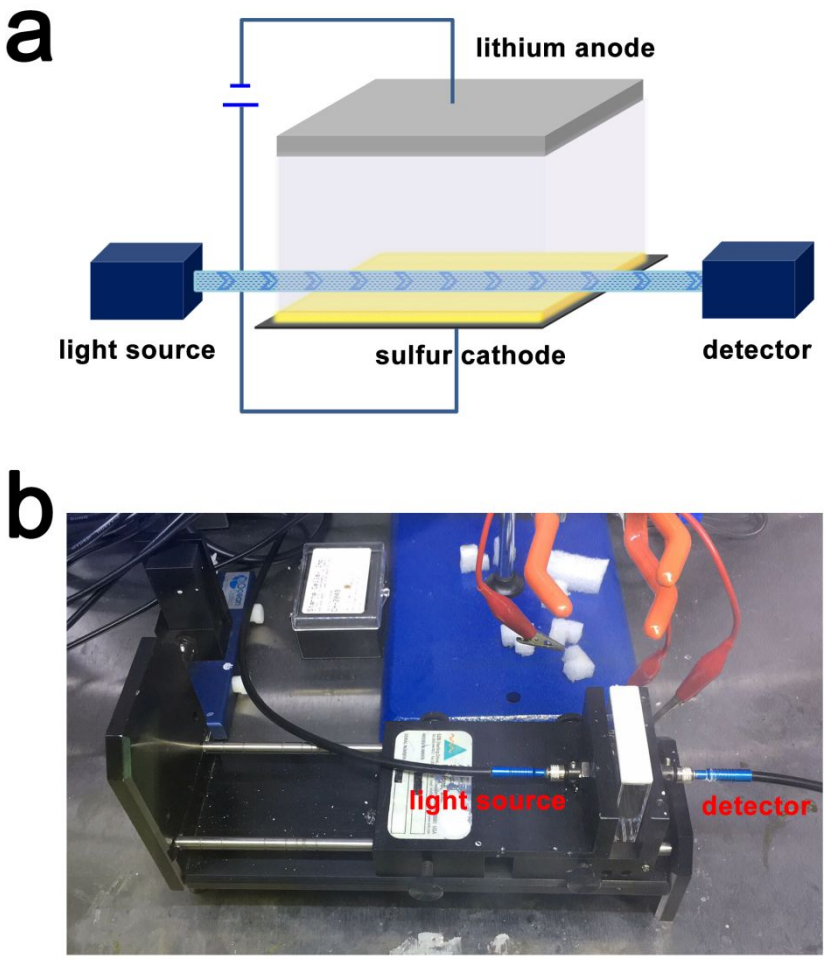

Figure S6. (a) Schematic of the *in-situ* UV-vis spectroscopy measurement setup and (b) a digital photo of the setup.

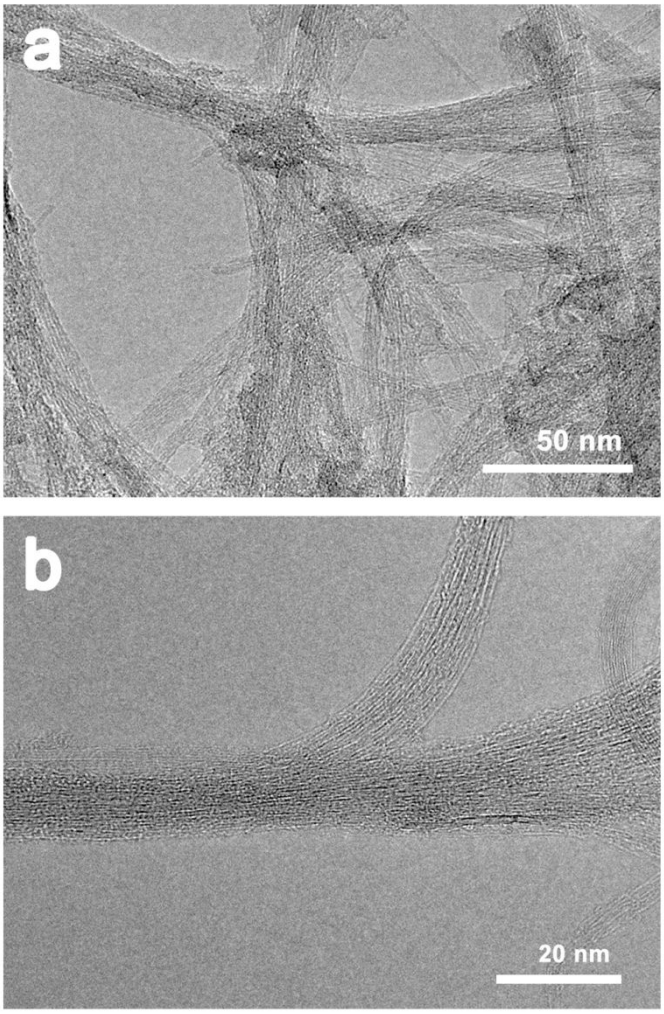

Figure S7. TEM images of CNT heated at 700 ^{o}C in hydrogen.

The 1D nanostructure entanglement not only inhibited the aggregation of Co_9S_8, but also increased the polysulfide encounter and the capture efficiency.

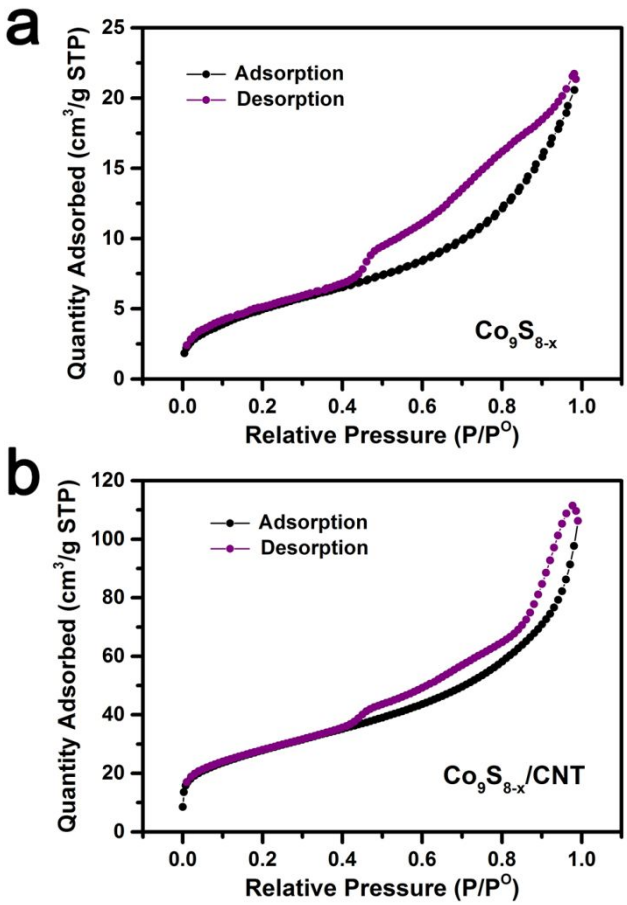

Figure S8. N_2 adsorption and desorption isotherms of (a) Co_9S_{8-x} and (b) Co_9S_{8-x}/CNT.

The surface areas of Co_9S_{8-x} and Co_9S_{8-x}/CNT are 18.94 m^2/g and 100.91 m^2/g respectively. The larger surface area of the latter may be attributed to the high surface area of CNT; and the CNT as the catalyst support to sustain a high dispersion of Co_9S_{8-x} nanoparticles without much aggregation (see TEM images in Figure 2b). The large surface area and better contact with polysulfides are conducive to the polysulfide conversion reactions.

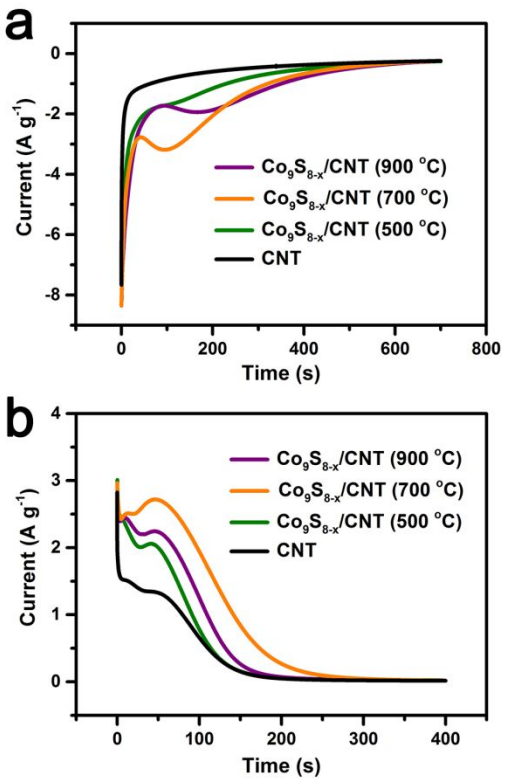

Figure S9. Evaluation of the polysulfide conversion kinetics on samples prepared at different temperatures. (a) Current time responses from potentiostatic discharge from the open circuit condition (2.2 V) to 2 V and (b) Current-time responses from potentiostatic recharge to 2.4 V.

The electrochemical properties of samples prepared at different temperatures can be deduced from their reaction kinetics with sulfur (or Li_2S). Potentiostatic discharge and recharge were used to evaluate the polysulfide conversion kinetics. The results are given in Figure S9 below. The current in potentiostatic discharge was contributed by the deposition of Li_2S on the catalyst (Figure S9a), while the current in potentiostatic charge was contributed by the deposition of sulfur on the catalyst (Figure S9b). Higher currents were measured from the Co_9S_{8-x}/CNT (700 ^oC) sample in both potentiostatic discharge and charge; indicating accelerated deposition kinetics of Li_2S and sulfur. The measurements confirmed the catalytic effects of sulfur deficiencies on both polysulfide reduction and oxidation reactions. Although Co_9S_{8-x}/CNT (900 ^oC) had more sulfur deficiencies on the surface, the high temperature treatment also caused more extensive particle aggregation to result in an overall poor electrochemical performance. Hence, the Co_9S_{8-}

$_x$/CNT (700 ^{o}C) sample with the next highest sulfur deficiency content was selected for detailed follow-up investigations.

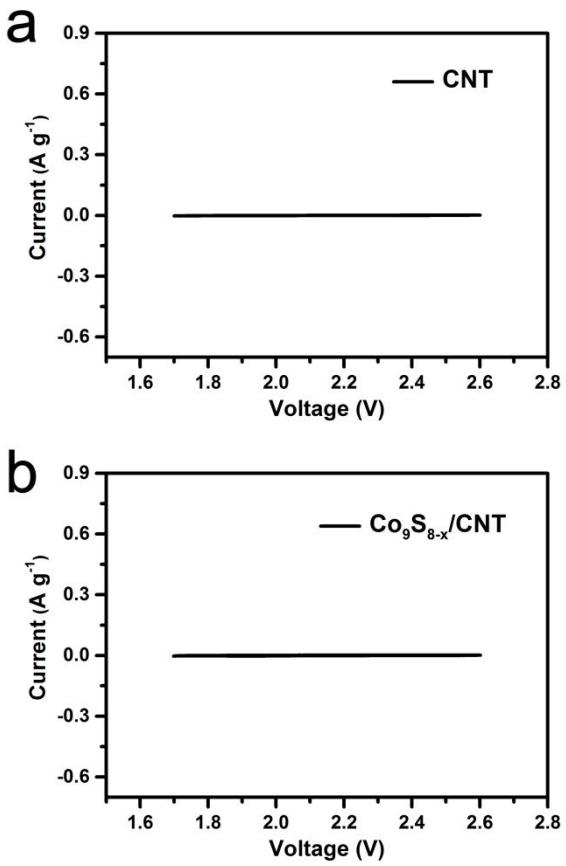

Figure S10. Cyclic voltammograms of the lithium-catalyst cells without polysulfide in the electrolyte at 0.1 mV s^{-1} in 1.7 V-2.6 V.

No peaks appeared in the cyclic voltammograms of lithium-catalyst cells without the polysulfide, indicating that Co_9S_{8-x} and CNT did not contribute to the redox reactions in Figure 3e.

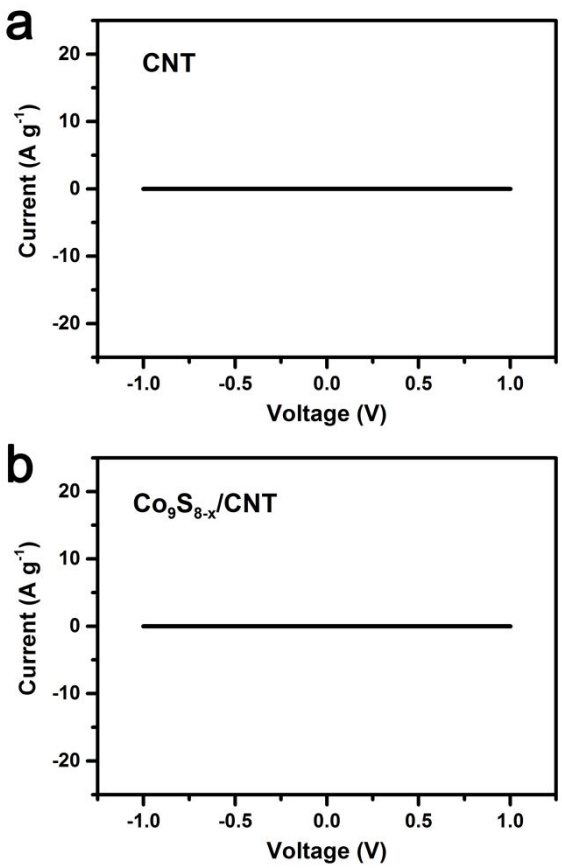

Figure S11. Cyclic voltammograms of symmetric cells without polysulfide in the electrolyte.

No peaks appeared in the cyclic voltammograms of symmetric cells without the polysulfide, indicating that the Co_9S_{8-x} and CNT did not contribute to the redox reactions in Figure 4a.

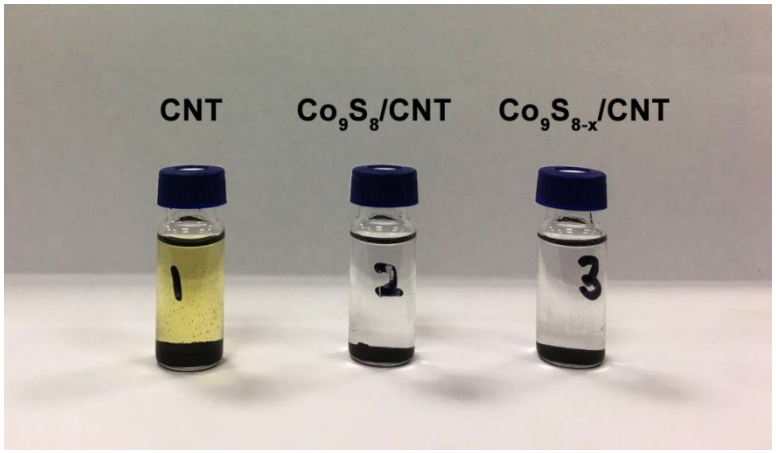

Figure S12. Adsorption uptake of Li_2S_6 solution (2.5 mmol L^{-1} in 1:1 (v/v) DME/DOL) by the same amount of Co_9S_8/CNT and Co_9S_{8-x}/CNT.

Both composites were equally adept at polysulfide uptake (Figure S12). However, the sulfur cathode with sulfur-deficient Co_9S_{8-x}/CNT delivered notably better performance in symmetric cells. Adsorption is the first step in overall catalysis; and the performance difference between Co_9S_8/CNT and sulfur-deficient Co_9S_{8-x}/CNT could only be caused by post-adsorption reaction steps.

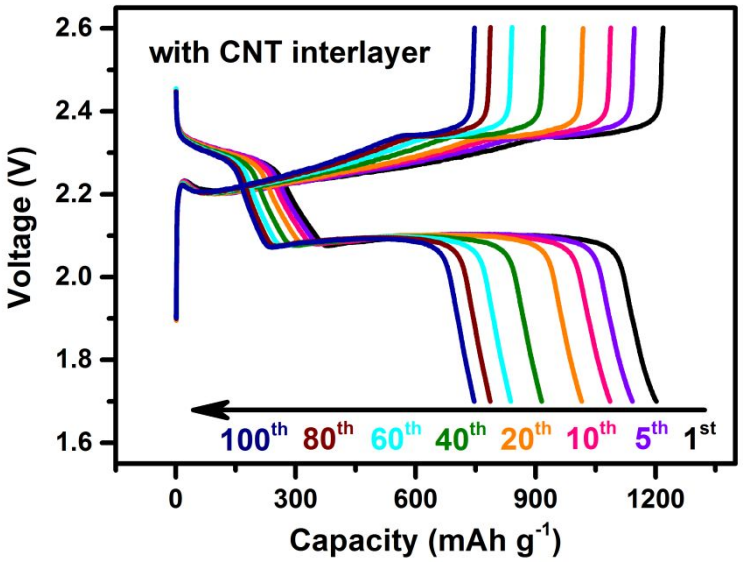

Figure S13. Galvanostatic charge-discharge curves of a lithium-sulfur battery with a CNT interlayer at 0.3 C for 100 cycles.

There were no redox features at ~1.9 V during discharge and at ~2.2 V during recharge, indicating that the redox features were only accessible in the presence of the Co_9S_{8-x} catalyst.

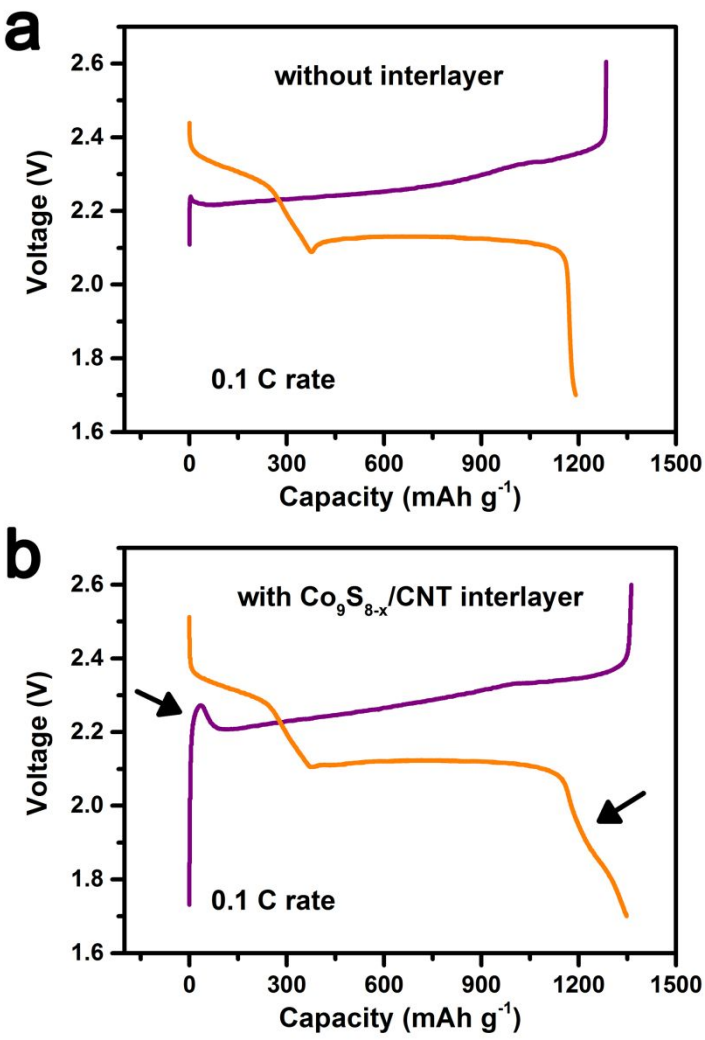

Figure S14. Galvanostatic charge-discharge curves of the lithium-sulfur battery with and without a Co_9S_{8-x}/CNT interlayer at 0.1 C.

The discharge plateaus at about 2.3 V and 2.0 V are typical of sulfur reduction to soluble long-chain polysulfides (Li_2S_x, $4 \leq x \leq 8$), and the formation of insoluble end products (Li_2S_2/Li_2S) respectively. The two plateaus in the charge curve at about 2.3 V and 2.4 V are reverse of these reactions which converted Li_2S_2/Li_2S to sulfur. There is clearly less potential hysteresis in the sulfur cathode with an integrated Co_9S_{8-x}/CNT interlayer.

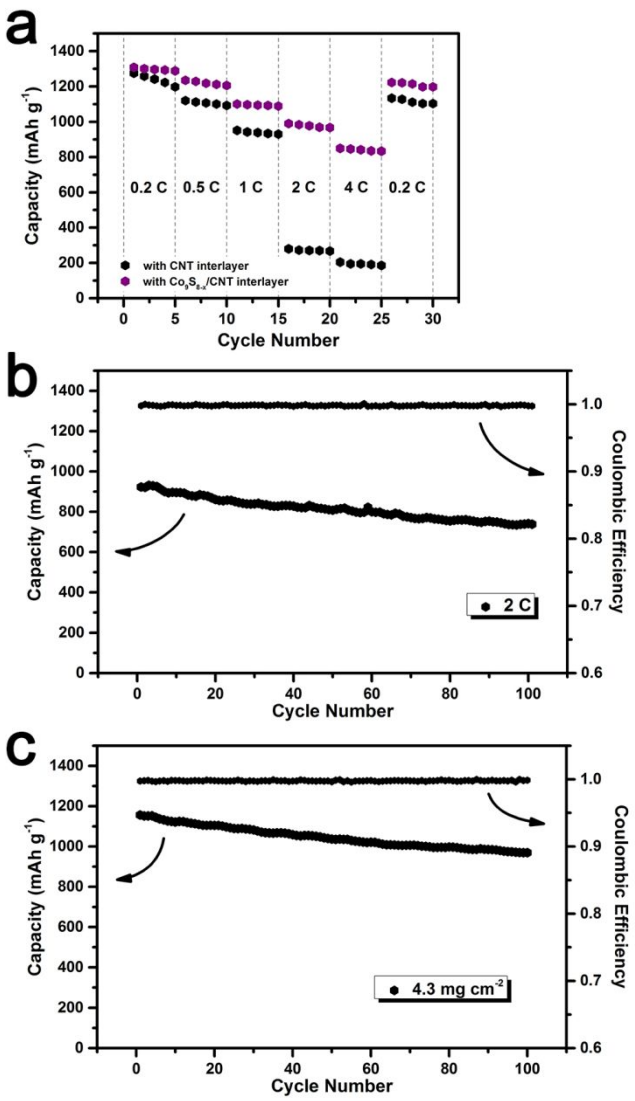

Figure S15. Electrochemical performances of lithium-sulfur batteries with a Co_9S_{8-x}/CNT catalytic interlayer. (a) Rate performance at different C-rates. Cycle stability (b) at the 2C rate and (c) with high sulfur-loading cathode at the 0.3C rate.

At the 0.2C rate, the initial discharge capacity of a sulfur cathode with the Co_9S_{8-x}/CNT catalytic interlayer was 1308.9 mAh g^{-1}, slightly higher than that of a sulfur cathode with the CNT interlayer (1274.9 mAh g^{-1}, Figure S15a). The capacity difference increased noticeably at higher C-rates. Consequently, a sulfur cathode with the Co_9S_{8-x}/CNT catalytic interlayer could deliver a much higher capacity (849.7 mAh g^{-1}) than a sulfur cathode with only a CNT interlayer (204.3 mAh g^{-1}).

The cycle stability of a Li-S cell with the Co_9S_{8-x}/CNT catalytic interlayer at the 2C rate is shown in Figure S15b. Cycle stability remained good even at this ten-fold increase in the C-rate (from 0.2C) - the Li-S cell could still provide 742.3 mAh g^{-1} of capacity after 100 cycles (80.4% initial capacity retention).

The Li-S cell with a high sulfur-loading cathode (4.3 mg cm^{-2}) and the Co_9S_{8-x}/CNT catalytic interlayer could also deliver 969.5 mAh g^{-1} after 100 cycles at the 0.3C rate (83.8% of initial capacity retention, Figure S15c).

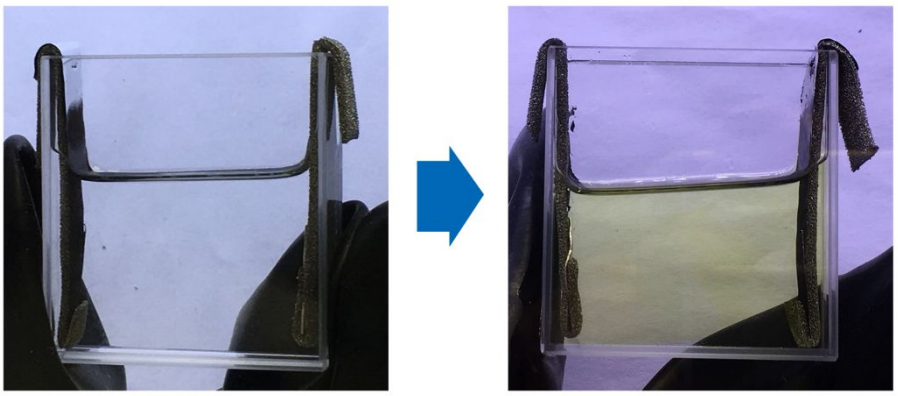

Figure S16. Photograph of the cell with sulfur cathode coated with CNT interlayer before and after test.

The CNT interlayer was unable to inhibit the diffusion of polysulfides from the cathode after the cell was discharged potentiostatically to 1.7 V for 12 min.

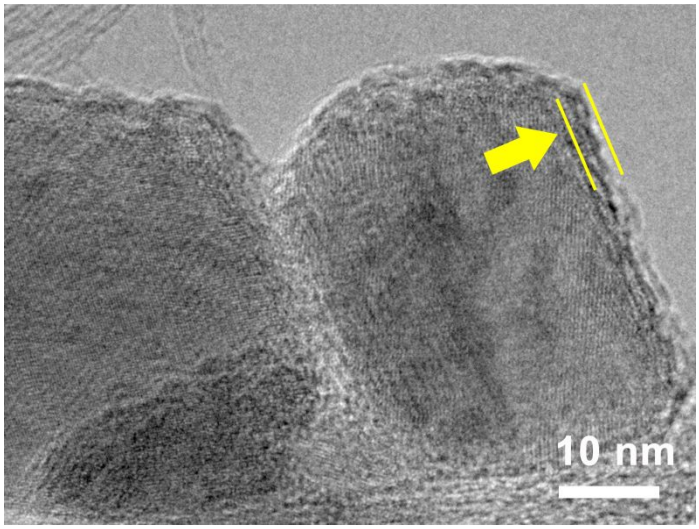

Figure S17. TEM image of the Co_9S_{8-x}/CNT in the cathode interlayer after 20 cycles.

Table S2 Comparison of the Co_9S_{8-x}/CNT interlayer with other lithium-sulfur battery interlayer in the literature.

Sulfur cathode interlayer	Initial capacity	Cycling performance	Capacity fade rate	Cathode (Sulfur wt%)	Reference
Ti_3C_2 Mxene nanosheets	899 mAh g^{-1} (0.5 C)	428.8 mAh g^{-1} after 200 cycles	0.26% per cycle	Ti_3C_2 Mxene nanoribbon/ Sulfur (47.6%)	1
nanocrystalline niobium carbide	1082 mAh g^{-1} (0.5 C)	872 mAh g^{-1} after 150 cycles	0.13% per cycle	sulfur (60%)	2
boron nitride nanosheets/ graphene	1100 mAh g^{-1} (1 C)	700 mAh g^{-1} after 1000 cycles	0.036% per cycle	sulfur (70%)	3
ultrathin MnO_2/graphene /carbon nanotube	960 mAh g^{-1} (1 C)	293 mAh g^{-1} after 2500 cycles	0.029% per cycle	Sulfur/CNT (60%-80%)	4
ultralight multiwall carbon nanotube/ N-doped carbon quantum dot	1330.8 mAh g^{-1} (0.5 C)	650.7 mAh g^{-1} after 500 cycles	0.102% per cycle	sulfur (54%)	5
WS_2/carbon cloth	1493.7 mAh g^{-1} (0.05 C)	1201 mAh g^{-1} after 100 cycles	0.19% per cycle	sulfur (70%)	6
laponite nanosheets/carbon black	1199.5 mAh g^{-1} (0.2 C)	838 mAh g^{-1} after 500 cycles	0.06% per cycle	sulfur (70%)	7
ZnO nanowires/Ni foam	712.5 mAh g^{-1} (2 C)	577.1 mAh g^{-1} after 500 cycles	0.038% per cycle	sulfur/MW CNT (70%)	8
Co_9S_{8-x}/CNT	1272.9 mAh g^{-1} (0.3 C)	648.5 mAh g^{-1} after 1000 cycles	0.049% per cycle	sulfur (70%)	this work

REFERENCES

(1) Dong, Y.; Zheng, S.; Qin, J.; Zhao, X.; Shi, H.; Wang, X.; Chen, J.; Wu, Z. S., All-Mxene-Based Integrated Electrode Constructed by Ti_3C_2 Nanoribbon Framework Host and Nanosheet Interlayer for High-Energy-Density Li-S Batteries. *ACS Nano* **2018,** *12*, 2381-2388.

(2) Cai, W.; Li, G.; Zhang, K.; Xiao, G.; Wang, C.; Ye, K.; Chen, Z.; Zhu, Y.; Qian, Y., Conductive Nanocrystalline Niobium Carbide as High-Efficiency Polysulfides Tamer for Lithium-Sulfur Batteries. *Adv. Funct. Mater.* **2018,** *28*, 1704865.

(3) Fan, Y.; Yang, Z.; Hua, W.; Liu, D.; Tao, T.; Rahman, M. M.; Lei, W.; Huang, S.; Chen, Y., Functionalized Boron Nitride Nanosheets/Graphene Interlayer for Fast and Long-Life Lithium-Sulfur Batteries. *Adv. Energy Mater.* **2017,** *7*, 1602380.

(4) Kong, W.; Yan, L.; Luo, Y.; Wang, D.; Jiang, K.; Li, Q.; Fan, S.; Wang, J., Ultrathin MnO_2/Graphene Oxide/Carbon Nanotube Interlayer as Efficient Polysulfide-Trapping Shield for High-Performance Li-S Batteries. *Adv. Funct. Mater.* **2017,** *27*, 1606663.

(5) Pang, Y.; Wei, J.; Wang, Y.; Xia, Y., Synergetic Protective Effect of the Ultralight Mwcnts/Ncqds Modified Separator for Highly Stable Lithium-Sulfur Batteries. *Adv. Energy Mater.* **2018,** *8*, 1702288.

(6) Park, J.; Yu, B.-C.; Park, J. S.; Choi, J. W.; Kim, C.; Sung, Y.-E.; Goodenough, J. B., Tungsten Disulfide Catalysts Supported on a Carbon Cloth Interlayer for High Performance Li-S Battery. *Adv. Energy Mater.* **2017,** *7*, 1602567.

(7) Yang, Y.; Zhang, J., Highly Stable Lithium-Sulfur Batteries Based on Laponite Nanosheet-Coated Celgard Separators. *Adv. Energy Mater.* **2018,** *8*, 1801778.

(8) Zhao, T.; Ye, Y.; Peng, X.; Divitini, G.; Kim, H.-K.; Lao, C.-Y.; Coxon, P. R.; Xi, K.; Liu, Y.; Ducati, C.; Chen, R.; Kumar, R. V., Advanced Lithium-Sulfur Batteries Enabled by a Bio-Inspired Polysulfide Adsorptive Brush. *Adv. Funct. Mater.* **2016,** *26*, 8418-8426.